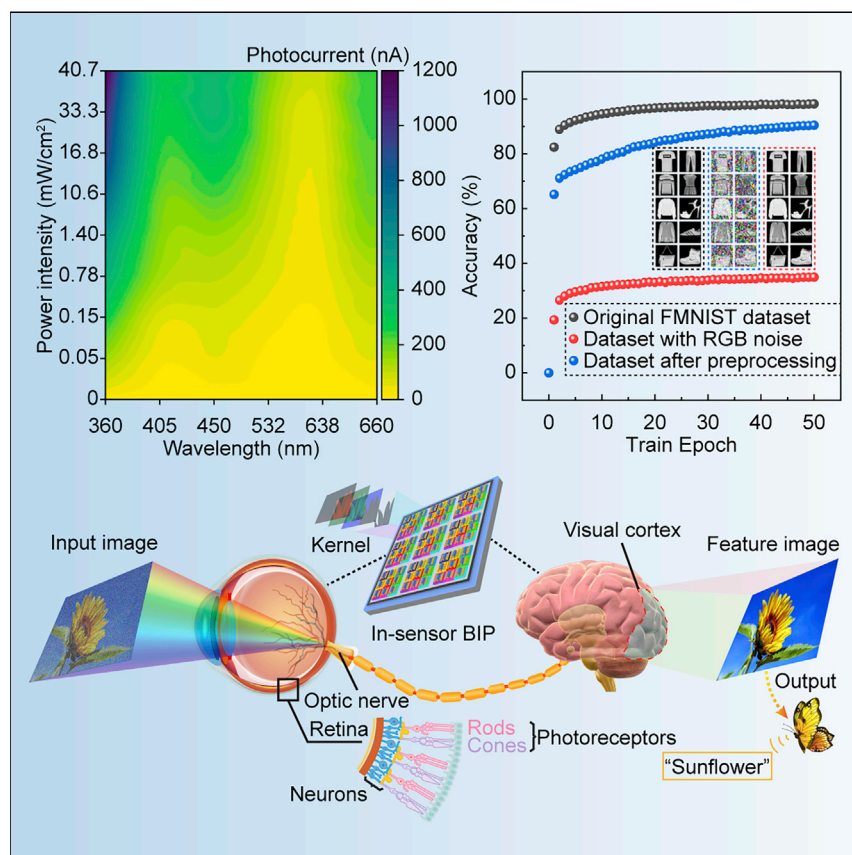# Matter

Article

Retina-inspired in-sensor broadband image preprocessing for accurate recognition via the flexophototronic effect

The flexophototronic effect has been realized in 2D MoS$_2$ devices fabricated by the 3D stress-stabilization process, and the flexophototronic-enhanced photosensors can achieve broadband sensing and high photoresponse for UV selection. Based on the arrays of opto-synapses, an artificial visual system integrating broadband perception, long-term memory, and broadband image preprocessing functions is developed.

Pengwen Guo, Mengmeng Jia, Di Guo, Zhong Lin Wang, Junyi Zhai

zhong.wang@mse.gatech.edu (Z.L.W.)
jyzhai@binn.cas.cn (J.Z.)

Highlights

3DSS process can achieve permanent polarization, integration, and practical application

The enhanced photosensors have realized broadband perception and high photoresponsivity

The light-dosage-tunable synaptic characteristics have been simulated by the sensors

An artificial visual system can perform preprocessing tasks for accurate recognition

Improvement
5
Enhanced performance with innovative design or material control

Matter

Article

Retina-inspired in-sensor broadband image preprocessing for accurate recognition via the flexophototronic effect

Pengwen Guo,[1,2,4] Mengmeng Jia,[1,2,4] Di Guo,[1,4] Zhong Lin Wang,[1,3,*] and Junyi Zhai[1,2,5,*]

SUMMARY

Neuromorphic visual systems are promising candidates for emulating vision perception and recognition tasks, especially for two-dimensional (2D) semiconductor-based imaging sensors due to their tunable electrical/optical properties and compatibility for heterogeneous integration. The device integration of sensing-memory-processing units and accurate recognition for image sensors become critical obstacles to simulating visual systems; thus, developing more advanced neuromorphic structures is required. Here, we demonstrate a retina-inspired 2D molybdenum disulfide (MoS_2)-based vision sensor capable of both broadband perception and preprocessing functions by exploiting the flexophototronic effect. Three-dimensional stress stabilization (3DSS) is consciously introduced into the flexophototronic sensor to achieve broadband sensing and high photoresponsivity, resulting in distinctive UV information extraction for image preprocessing. Furthermore, the artificial neural network can remarkably enhance the recognition accuracy from 35% to 90% due to preprocessing validity. This work lays the foundation for developing emerging flexophototronics for artificial visual systems endowed with real-time interaction and efficient execution.

INTRODUCTION

Vision, sound, smell, taste, and touch are the primary exteroceptions that human beings can perceive and interpret,[1,2] enabling their awareness of external stimuli. Over 80% of the information from the surrounding environment is detected by the visual sense, hence the retina is crucial to human perception.[3–5] As the retina containing sensory neurons can not only perceive light signals but also preprocess images before transferring more complicated visual information to the visual cortex, vision is essentially a memory-based process.[6] An artificial intelligence visual system based on the complementary metal-oxide-semiconductor (CMOS) technology consists of a photoreceptive chip to perceive and convert the visual inputs to digital signals, a memory unit to store visual data, and an artificial neural network (ANN) to conduct complex tasks for image processing.[7] Compared with the human visual system, existing artificial visual systems generate large amounts of redundant data due to the physical separation of the functional units and, subsequently, lead to significant energy consumption and data access delays when performing unstructured image recognition. Additionally, bandwidth restriction makes it challenging to swiftly relay full data back to central or cloud computers to achieve information processing in real time due to the increasing proliferation of sensory nodes.[5,7,8] Therefore, developing multifunctional electronics that integrate sensing, memory, and processing

PROGRESS AND POTENTIAL

Flexoelectricity, the coupling between electric polarization and the strain gradient, widely exists in dielectric and semiconductor materials in any space group. In this work, a novel 3D stress-stabilization process has been developed to generate permanent polarization in 2D MoS_2. The photosensors enhanced by the flexophototronic effect can achieve broadband perception and high photoresponsivity. Moreover, based on the photosensors array, an artificial visual system is developed to extract UV information from the environment and perform broadband image preprocessing functions with high frame rate and low energy consumption, thus remarkably improving the image recognition accuracy. This work paves a path for developing emerging flexophototronics for artificial visual systems endowed with real-time interaction and efficient execution.

functions is a prospective strategy for the implementation of highly effective artificial visual systems.[9–12]

In addition to developing in-sensor processing functions, the majority of previous studies concentrate on the exploitation of neuromorphic sensors working in the visible band, which are intended to be substitutes for a human visual system. It is worthwhile to note that plenty of animal species can recognize and utilize UV spectra to maintain essential behaviors and communications. For example, butterflies own one of the broadest visual ranges of any animal alive, and their ability to sense under UV light helps them locate healthy mates and optimize nectar supply.[13] Also, European rollers can identify the health status of chicks in their brood by employing UV light and formulating an appropriate food allocation strategy,[14] and hedgehog as a nocturnal mammal has also been shown to utilize UV to help them navigate at night, collect food, and detect potential predators.[15] Considering the limited wavelength of human perception, the development of broadband neuromorphic sensors containing UV light can significantly enhance human visual perception capabilities, which are widely explored for the applications in the fields of healthcare, secure communication, and flame detection, among others. The reported neuromorphic memories are mostly three-terminal transistors, where the floating-gated memories rely on charge tunneling in the floating-gate layer to realize memory function, resulting in slow response time and complex multilayer architectures,[16–18] whereas the ion-gated memories[19,20] suffer from poor endurance due to the frequent intercalation/deintercalation of ions into single-crystal two-dimensional (2D) semiconductor channels, which may damage the channel lattice[19] and consume more energy than the biological level.[21] Emerging two-terminal photonic synapses for 2D materials that combine the high optoelectronic performances and electric neuromorphic modulation and computation could pave the way for neuromorphic sensors with broad bandwidth, fast speed, low cross-talk, and low energy consumption.[22]

Molybdenum disulfide (MoS_2) as one 2D semiconductor has become a potential candidate for next-generation optoelectronics due to its tunable band gap, high carrier mobility, and thermal-chemical stability.[23] Considering that the interface barrier of MoS_2/graphene contact can induce persistent photoconductivity[24] and that a strong flexotronic effect has been proven to exist in 2D MoS_2,[25] utilizing flexophototronic polarization as a "gate" to modulate the barrier can realize multifunctional opto-synapses with outstanding performance. The mechanism of the flexophototronic effect is analogous to the piezophototronic effect,[26,27] when an inhomogeneous strain is applied to a semiconductor, the localized polarization charges induced by flexoelectric can effectively modulate the generation, separation, transport, and recombination of photogenerated carrier nearby barrier or junction area, which is the mechanism of the flexophototronic effect. Moreover, multilayer MoS_2 have broader spectral response, such as from UV to near-infrared (NIR) wavelengths,[28] than single-layer MoS_2 due to the narrower band gap. These effects suggest that outstanding photodetection properties existing in 2D MoS_2 flexophototronics can realize UV opto-synaptical basic behaviors. However, electromechanical modulation for the conventional stress/strain sensors based on the sensing mechanism of flexoelectric[29,30]/piezoelectric[31,32]/piezoresistive[33,34] effects must be achieved by applying an external force or bending the substrate. The instability of load force for these devices might be not as efficient at providing sufficient continuous power/modulation and may even induce mechanical failure in materials; moreover, mechanical modulation manners independent of sensing systems severely limit the integration and practical applications for those traditional electromechanical systems.

[1]Beijing Institute of Nanoenergy and Nanosystems, Chinese Academy of Sciences, Beijing 101400, P.R. China

[2]School of Nanoscience and Technology, University of Chinese Academy of Sciences, Beijing 100049, P.R. China

[3]Georgia Institute of Technology, Atlanta, GA 30332, USA

[4]These authors contributed equally

[5]Lead contact

*Correspondence:
zhong.wang@mse.gatech.edu (Z.L.W.),
jyzhai@binn.cas.cn (J.Z.)

https://doi.org/10.1016/j.matt.2022.11.022

Matter
Article

CellPress

In this work, we report the development of a retina-inspired vision system using the flexophototronic synapse with UV extraction function to realize image preprocessing for accurate recognition. A novel 3D stress-stabilization (3DSS) process by controllably patterning substrate as beamed morphology is precisely designed with strain-gradient engineering to significantly improve the carrier mobility/photoresponsivity in 2D semiconductors and break through the application limitations for traditional electromechanical modulation. The photosensors are enhanced by the 3DSS process to simultaneously achieve broadband perception (UV-visible), high photoresponse ($2,952$ A W^{-1} at 48 μW cm^{-2}, 3,672% outperforming unenhanced sensor). The opto-synaptic characteristics, such as neural facilitation and long-term plasticity, are realized under the light pulses embodying spatiotemporal information (e.g., illumination time and intensity). Based on the simulating synaptic sensing and memory functions at the device level, an ANN is built to perform the tasks of image recognition. The artificial visual system is capable of extracting featured UV information from its surroundings and performing broadband processing functions with a high frame rate (100 frames per second [FPS]) and low energy consumption (77.28 fJ) to remarkably improve the image recognition accuracy on the Fashion-MNIST image classification dataset from 35% to 90% due to the large enhancement of the photoresponse.

RESULTS AND DISCUSSION

Image processing of the retina

Visual information is processed by the visual cortex of the cerebral cortex for a human brain. An image input originating from the photoreceptors in the retina travels through the optic nerve and then reaches the visual cortex for processing. Lastly, the processed information is transferred to other areas of the brain for analysis and utilization. This extremely professional mechanism enables the brain to recognize the image rapidly without much conscious effort (Figure 1A). Rods are photoreceptors in the retina that are specialized for functioning at low light levels. Cones are photoreceptors located in the middle of the retina and perceive color and visual sharpness. They are responsible for daylight vision or bright light, as well as detailed vision. There are three types of cones, namely red-sensing cones that make up 60% of the total cones in the retina, green-sensing cones that make up 30%, and blue-sensing cones that make up 10%. Inspired by the visual system containing the retina and visual cortex, we are attempting to exhibit neuromorphic vision sensors with integrated visual sensing and image recognition, and the schematic drawing of the in-sensor broadband image preprocessing (BIP) is displayed in Figure 1B. The sensor is primarily fabricated by stacking 2D MoS_2 and few-layered graphene (FLG) into a photosensing heterostructure employing mechanical exfoliation of high-quality single crystals and a controlled dry-transfer process. More details about device fabrication can be found in the experimental procedures. During the light-signal transmission, the vision sensor can be considered an artificial opto-synapse, where an electric spike is generated with a light pulse inputting.

The energy consumption during one opto-synapse event is primarily determined by the intensity and width of the incident light pulse, meaning that energy consumption can be reduced by modulating light intensity for a fixed-width light pulse. However, the height of output electric spike under weak illumination is difficult to identify, so a high photocurrent response enhanced by the flexophototronic effect is of important significance to realizing ultralow power opto-synapse. Firstly, multilayer MoS_2 has a broader spectra response than single-layer MoS_2 for its narrower band gap, and FLG as a semimetal can also increase the response wavelengths and reduce the Schottky
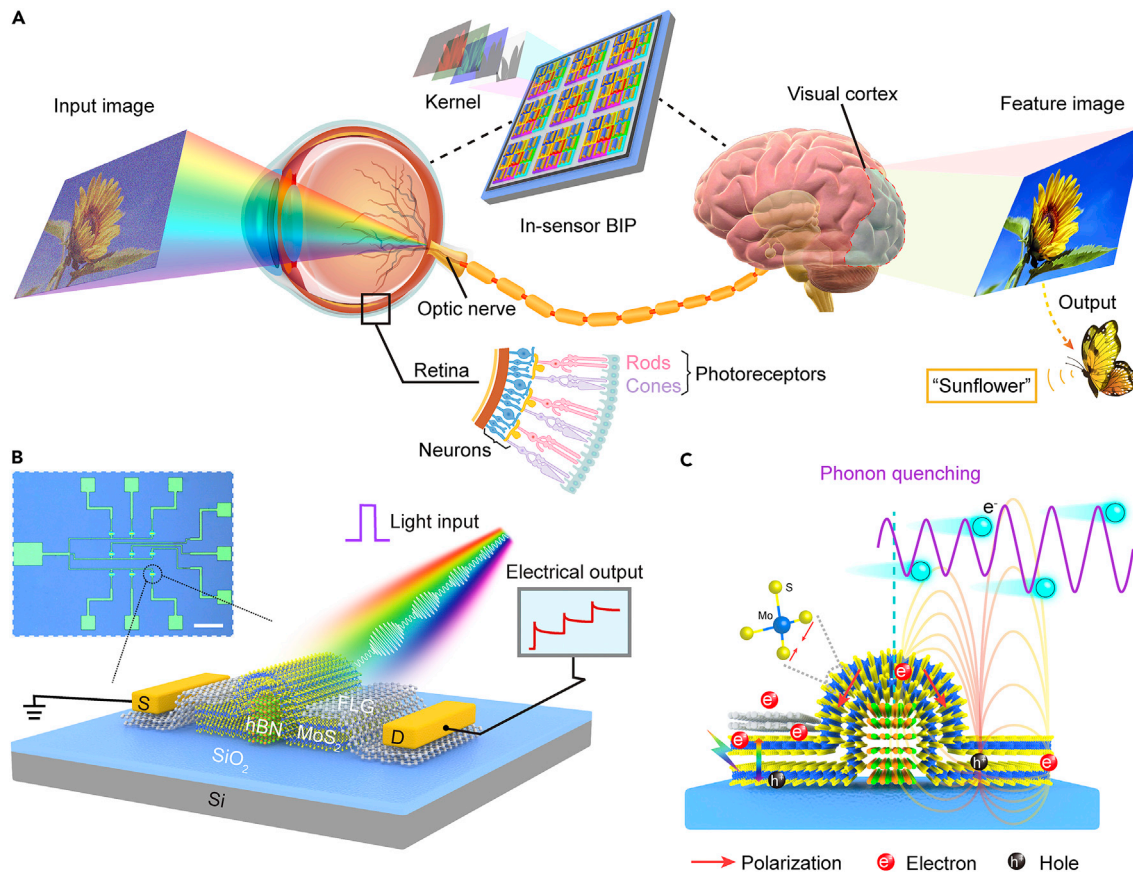
Figure 1. Image processing of a retina

(A) The visual cortex can recognize flower species after the flower image sensed by photoreceptors in the retina.

(B) Schematic of device structure of MoS_2 vision sensor. The inset shows an optical image of the photosensors array. Scale bars: 100 μm.

(C) Illustration of the 3DSS-induced lattice distortion results in an increased electric polarization that improves dielectric screening and concurrently quenches electron-proton (E-P) scattering, which drastically boosted carrier mobility. The electric-field lines between positive and negative charges depict the strength of dielectric screening. The purple solid lines represent phonon vibrations.

barrier[35] for an FLG/MoS_2/FLG lateral heterostructure. When the light is turned off, the potential barrier of MoS_2/FLG at the forward-biased terminal increased by the flexoelectric field hinders the photogenerated electrons from totally diffusing back to MoS_2 (as Figure S2D and the left section of Figure 1C show), and hBN as part of substrate can prevent a conductivity decrease due to photogenerated carriers trapped by the defect states, resulting in persistent photoconductivity,[36] which is helpful for simulating the decay characteristic of biological synapses.[24] Based on the 3DSS process, both edges of the hBN microbeam exhibit maximum strain gradients, which induces exacerbating curvature for the MoS_2 flake and causes the large lattice distortion in MoS_2 crystal. Attributed to the breaking of lattice symmetry, the electric polarization is enhanced in the crystal structure, and the increased electric polarization also enhances scattering from polar optical phonons at room temperature, thus improving the carrier mobility instead.[37] This is the micro-mechanism of the 3DSS (as the right section of Figure 1C shows), which differs from strain engineering but can further expand band-tunable property for the MoS_2 photosensor (Table S1; Note S1). In short, compared with typical MoS_2-based artificial opto-synapses, the flexophototronic opto-synapse exhibits advantages over broadband photosensing (UV to visual), high PSC, and low depression velocity via the 3DSS effect.
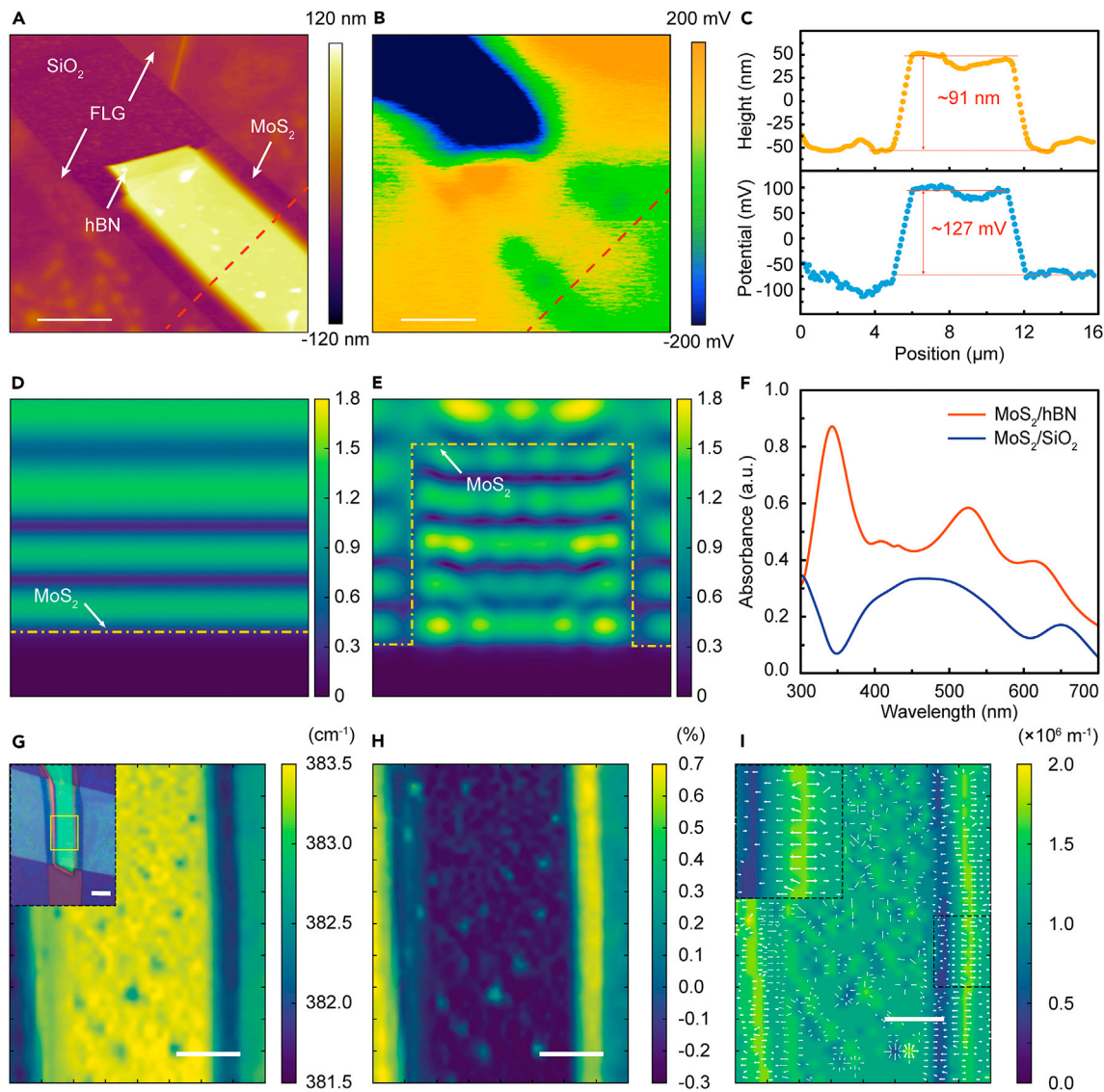
Matter
Article

CellPress

Figure 2. 3DSS effect in 2D MoS$_2$

(A and B) Height mapping (A) and surface potential mapping (B) of the MoS$_2$ nanoflake on the beamed-hBN/SiO$_2$ substrate.

(C) Height (top) and surface potential (bottom) cross-section of the orange and blue solid lines in (A) and (B).

(D and E) Electric-field cross-section distribution of (D) flat substrate and (E) beamed substrate under 360 nm irradiation.

(F) The absorbance of MoS$_2$ nanoflakes on flat SiO$_2$ substrate and beamed-hBN/SiO$_2$ substrate by FDTD solution simulations.

(G) Raman mapping of E_{2g}^1 mode of strained MoS$_2$ consisting of a thin MoS$_2$ flake lying on a hBN microbeam and two FLGs as contacts. The inset shows an optical image (mapping area) of this device.

(H) Strain map of the MoS$_2$ sheet calculated from (G).

(I) Map of strain-gradient value (color) and vector (arrows) in the MoS$_2$ sheet calculated from (H). Maximum strain gradients in the MoS$_2$ sheet are located at both edges of the microbeam with opposite directions. The inset is an enlarged view of the black dashed rectangle.

Scale bars in (A and B): 5 μm; in (G–I): 2 μm; in (G) inset: 5 μm.

3DSS effect in 2D MoS$_2$

The scan image by atomic force microscopy (AFM) in Figure 2A displays the thicknesses of the MoS$_2$ nanoflake, the FLG sheets, and the hBN microbeam. However, the distribution of the surface potential for the MoS$_2$ nanoflake somewhat does not correspond to the thickness in Figure 2B, which is common for van der Waals stack heterostructures due to interlayer defects and organic residues that are

retained by the Scotch tape during the mechanical exfoliation process. The contact potential difference (V_{CPD}) between the Pt/Ir-coated tip and the sample surface can determine the work function of MoS$_2$ nanoflake, where V_{CPD} can be expressed as

$$V_{CPD} = (\varphi_{tip} - \varphi_{sample})/e, \qquad \text{(Equation 1)}$$

where φ_{tip} ($\sim$5.7 eV) and φ_{sample} are the work functions of the tip and sample, respectively. Then, the work function difference $\Delta\varphi_{MoS2}$ between the unstrained MoS$_2$ and the strained MoS$_2$ can be calculated by

$$\Delta V_{CPD} = V_{CPD-s} - V_{CPD-u} = (\varphi_{tip} - \varphi_{strained})/e - (\varphi_{tip} - \varphi_{unstrained})/e$$

$$= (\varphi_{unstrained} - \varphi_{strained})/e = -\Delta\varphi_{MoS_2}/e \qquad \text{(Equation 2)}$$

Considering the ΔV_{CPD} of ≈ -127 mV between the strained or not MoS$_2$ nanoflakes in Figure 2C, the work function difference of both MoS$_2$ can reach $\sim$127 meV, which indicates a change in the FLG-MoS$_2$ Schottky barrier height (SBH) ($\Delta\varphi_B$) if regarding graphene as a semimetal (Figure S2C); in addition, analogous to the piezoresistive effect, a decrease in the band gap at a rate of $\sim$120 meV per percent strain[38] for a tensile multilayer MoS$_2$ is seen, meaning that the value of strain for the MoS$_2$ nanoflake can be up to $\sim$1.06%, which provides a large strain gradient in the out-of-plane direction due to the local strain locating in such a small dimension, namely the height of hBN microbeam is $\sim$91 nm (Figure 2C).

To further explore the mechanism of enhancing the performance of MoS$_2$ heterostructure via 3DSS effect, the electric-field distributions of MoS$_2$ nanoflakes on the flat and beamed substrate were obtained from finite-difference time domain (FDTD) simulation as shown in Figures 2D and 2E , respectively. And the 3D model can be constructed based on the shape and size of the device in Figure 1B. Furthermore, in order to intuitively compare the electric-field distribution of various substrate structures and illuminations, the color bars of the electric-field diagrams have been appropriately adjusted. Figures 2D and 2E show the electric-field distribution in a cross-section on the flat substrate and beamed substrate under vertical irradiation with a 360 nm laser, respectively, and these two substrates are deposited by MoS$_2$ nanoflakes of about four layers. Compared with the flat substrate, the field strength around the MoS$_2$ nanoflake for the beamed substrate device obtains a significant enhancement, which can be explained by the strengthened scattering for photons at the interface between the MoS$_2$ nanoflake and the beamed substrate with the hBN microbeam. In addition, tensile strain is introduced to the MoS$_2$ nanoflake on the beamed substrate, and the photons will drift from the bottom to the low-band-gap region due to the exciton funnel effect,[39] hence the photon accumulation around the microbeam can be observed as Figure 2E shows. The electric-field distributions for MoS$_2$ nanoflakes under various wavelength illuminations were also simulated in Figure S3, where the effect of photon accumulation around the microbeam under UV irradiation obtains exceed enhancement over other situations, which could be attributed to the fact that local polarization for the electrons occurs easily under high-energy photons excitation, and then the photons pairs are concentrated in MoS$_2$ and the microbeam region.[40] Furthermore, the spectrum absorption of MoS$_2$ nanoflakes on different substrates can also be obtained by calculating the reflectance and transmittance for the 3D model, and the results in Figure 2F demonstrate that the MoS$_2$ nanoflake on the hBN beamed substrate has better spectrum absorption under UV irradiation, which indicates the feasibility of the 3DSS process to achieve band tunability and UV detection for the MoS$_2$ photosensor.

Matter
Article

The confocal Raman characterization is used to study the structure of a van der Waals stack heterostructure for the sensor; the Raman spectra of the various layered materials involved in fabricating the device are shown in Figure S4A. In addition, a significant redshift of the E_{2g}^1 mode for the MoS$_2$ nanoflake can be found for the laser spots A to C in Figure S4C, which means that tensile strain and strain gradient exist in MoS$_2$ nanoflakes on the edge of the hBN microbeam. The Raman mapping of the E_{2g}^1 mode for MoS$_2$ in Figure 2G exhibits an intuitive redshift distribution, which accords with the inset optical image presented. Considering the E_{2g}^1 mode of the MoS$_2$ flake above four-layer approaches constant[41] (383.5 cm^{-1} for this situation), the region without strain (on the surface of the hBN microbeam here) can be regarded as a reference to calculate the strains and strain gradients for the MoS$_2$ nanoflake, which is based on the E_{2g}^1 shift as a function of uniaxial strain value (-1.7 cm^{-1} per percent strain[42]). The strain mapping in Figure 2H shows that tensile strain existing on the edge of the hBN microbeam can reach 0.7%, which corresponds to the analyzed result in Figure 2C, and that the calculated strain deviation between the surface potential difference and the Raman shift of the E_{2g}^1 mode is reasonable; these results indicate the effectiveness of the 3DSS (Note S3). Moreover, the reason that the surface of the microbeam has no strain may be that the MoS$_2$ tightly attaches to the top surface of a wide microbeam. The maximum strain gradient (nearly 2×10^6 m^{-1}) also appears on the edge of the microbeam in opposite directions, as Figure 2I and its enlarged view show, indicating the feasibility of controllably realizing permanent polarization by the 3DSS process.

Photoresponse characteristics enhanced by the flexophototronic effect

The optoelectrical properties of the MoS$_2$-based photosensor were studied to detect its photoresponse performance under various wavelengths and illumination intensities; the detailed experiment conditions are described in the experimental procedures. The electrical characterization was repeated in the 48 to 40.70 mW cm^{-2} range with a UV laser (360 nm). The I_{ds}-V_{ds} curves shown in Figure 3A are symmetric and have a weak Schottky contact feature due to the barrier being reduced by FLG and demonstrate a remarkable increase with orders of magnitude for drain current under illumination. Figure S5 also shows the strong light-dependent properties for the MoS$_2$-based photosensor under other band illuminations. The I_{ds}-V_{ds} curves resemble a Schottky contact, as the bias voltage extended from 0.1 to 10 V, which can be attributed to the enlarged effect of asymmetrical contact in the source and to drain. Based on a comparable increasing tendency, a small bias voltage (0.1 V) was chosen as operating voltage to avoid the device destruction by high current. Photocurrent (I_{ph}) is one of the metrics to evaluate the photoresponse and other performances for photosensors, which be expressed as

$$I_{ph} = I_{illumination} - I_{dark}, \qquad \text{(Equation 3)}$$

where the illumination current ($I_{illumination}$) and the dark current (I_{dark}) have been exhibited in Figure 3A. The comprehensive mapping for photocurrent in the MoS$_2$ photosensor under different illumination wavelengths and intensities has been plotted to further explore the photoresponse from UV to visual spectra (Figure 3B). All photocurrents under different illumination wavelengths exhibit intensity dependence, which indicates the photosensitized characteristics of the MoS$_2$ heterostructure and the wider spectral response for multilayer MoS$_2$ compared with monolayer. Moreover, the MoS$_2$ heterostructure exhibits a strong response for specified laser spectra, such as 660 (red), 532 (green), 450 (blue), and, especially, 360 nm (UV), which resembles the absorbance of the MoS$_2$ on the hBN substrate (Figure 2F). The photoresponse distinction to various featured bands is the foundation of enhancing image recognition by in-sensor BIP. The strain gradients in MoS$_2$
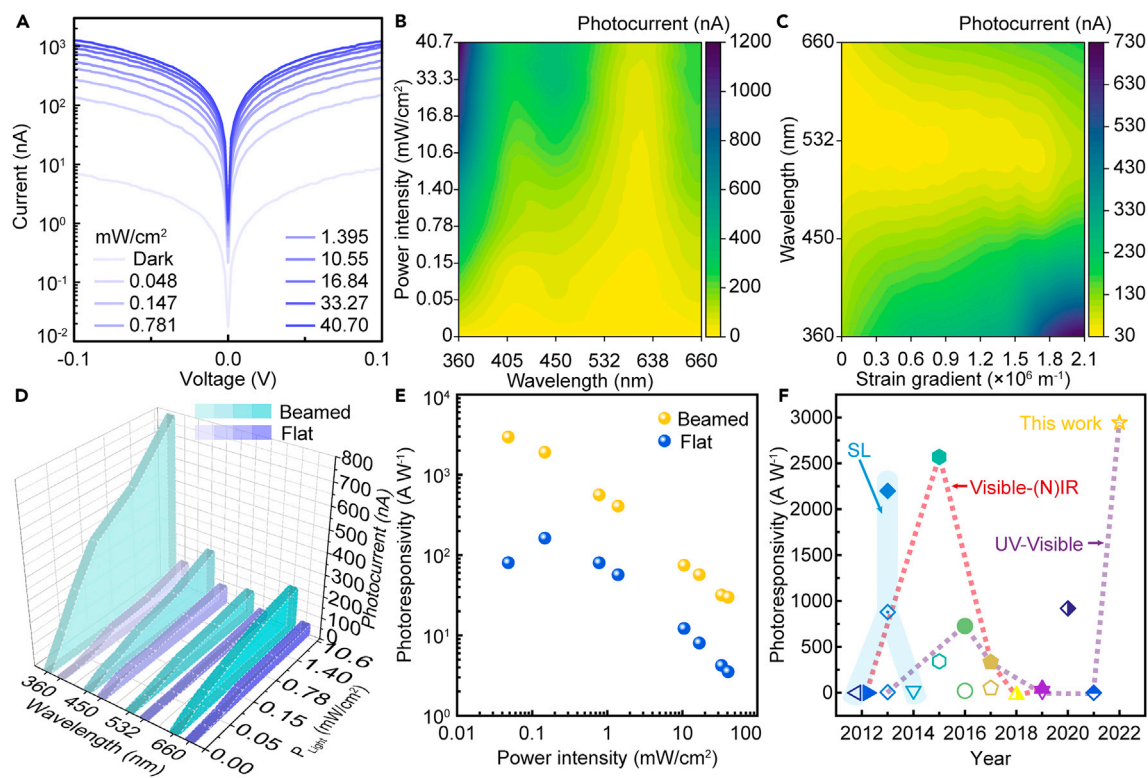
Figure 3. Photoresponse characteristics of the MoS$_2$ photosensors enhanced by the flexophototronic effect

(A) Output characteristics measured under various illumination intensities (dark to 40.70 mW/cm^2).

(B) A comprehensive photocurrent mapping for the MoS$_2$ sensors under different illumination wavelengths and intensities. The maximum strain is ~0.7%, and the color gradient represents the photocurrent.

(C) A comprehensive photocurrent mapping for the MoS$_2$ sensors under four feature bands illumination. The calculated strain gradients are from 0 to 2 × 10^6 m^{-1}.

(D and E) The intensity (D) and photoresponsivity (E) comparison of photocurrent for the flat and beamed (strain, ~0.7%) MoS$_2$ device under different illumination wavelengths and intensities.

(F) The photoresponsivity comparison for various types of MoS$_2$-based photosensors.

nanoflakes were introduced by the 3DSS process to explore the contribution of the flexophototronic effect to photocurrents, and comprehensive photocurrent mapping for the MoS$_2$ sensors under four feature band illuminations has been plotted in Figure 3C, where the calculated strain gradients are from 0 to 2 × 10^6 m^{-1} (on the flat substrate, meaning no strain gradient) for ~4 L MoS$_2$ device. The result shows that the photocurrents were significantly enhanced with strain gradients increasing due to the flexophototronic effect. It should be noted that the thicknesses of the hBN microbeams have nonlinear modulation for the photoresponse enhancement (Figure S6; Note S4), which is attributed to strain-gradient engineering and differs from the strain engineering. Next, based on the wide spectral response of the MoS$_2$ heterostructure, the photoresponse of the MoS$_2$ sensors on the beamed or flat substrate was compared under various illumination intensities. Figure 3D shows that the intensity comparison of the photocurrent for both sensors under the illumination of four feature bands has been plotted to intuitively comprehend the effect of flexophototronics. Compared with the flat substrate, the MoS$_2$ on the beamed substrate observed a significant increase in photocurrent at +0.1 V bias voltage, and the ratio of photocurrents can reach ~6.4 times under a 360 nm (10.6 mW cm^{-2}) laser illumination. To compare the response of the photocurrent, the photoresponsivity of the devices is defined as $R = I_{Ph}/P_{Light}$, where P_{Light} is the power density of incident

CellPress

light on the photosensor. As Figure 3E shows, the MoS_2 photosensor can reach a photoresponsivity of 2,952 A W^{-1} under a low light intensity (0.048 mW cm^{-2}); the reduction in photoresponsivity at higher light intensities may be attributed to the trap states that exist inside MoS_2 nanoflakes or at the interface between MoS_2 and the substrate.[43] Finally, we evaluate the photoresponsivity of the different types of MoS_2-based photosensors, and the results are plotted in Figure 3F (refer to Table S2). Single-layer MoS_2 as a direct band-gap semiconductor enables a high absorption coefficient and efficient electron-hole pair generation under photoexcitation, and its devices have high photoresponse in the visible range, whereas multi-layer MoS_2 obtains a wider spectral response due to its narrower band gap, and our flexophototronics-enhanced 2D MoS_2 photosensor performs with a high response to broadband spectrum from UV to visible light; moreover, other parameters such as the external quantum efficiency (EQE) and the detectivity (D*) for our sensor (Figure S7) are also far outperforming conventional MoS_2-based photodetectors (Table S2). These excellent performances of our photosensors indicate the validity of the 3DSS and laying a solid foundation for neuromorphic sensors.

Light-dosage-tunable synaptic behaviors

In general, the photoresponse time of conventional MoS_2-based photosensors is comparatively slow for practical applications. However, the sensor with persistent photoconductivity in this work (Figure S9; Note S5) is helpful for simulating the decay characteristic of biological synapses. Under appropriate stimuli, a presynapse in a biological synapse can deliver excitatory or inhibitory neurotransmitters that can bind to receptors on the postsynapse, which induces a postsynaptic current (PSC) to accomplish signal transmission,[21] and the synaptic weight (w) can be considered channel conductance (ΔPSC). Accordingly, this mechanism can be simulated by the charge transmission characteristics for in-sensor BIP, which is modulated by the light pulse as the input spike (Figure 4A). The transient photoresponse of the MoS_2 broadband sensor is shown in Figure 4B, demonstrating selectivity to different light wavelengths, and it is clear that the photosensor indicates a higher ΔPSC value under 360 nm illumination (other ΔPSCs under various wavelength light pulses are shown in Figure S8), which corresponds to the spectra dependence for the absorbance of the MoS_2 heterostructure (Figure 2F). Therefore, this band light pulse was used as an input spike to simulate synaptic behaviors and realize a UV selection function for our enhanced artificial visual system (Note S7).

Figure 4C shows the photoresponse of the sensor to light pulses ranging in intensities from 0.048 to 40.70 mW cm^{-2}, and the photocurrent promoted from 168 to 789 nA (V_{ds} = +0.1 V) with increasing light intensity. Hence, the sensor as an opto-synapse can realize dynamic modulation output of the photocurrent by changing the wavelength and intensity of the illumination, which is crucial to broadband information processing. As the illumination is switched out, each current decreases slightly and tends to remain in a stable photoconductivity state (Figures 4D and S10), presenting repeatable long-term potentiation (LTP) behavior (about a few minutes to hours),[44] as long-term plasticity, which is a fundamental function for biological synapses realizing memory and learning. One more thing to note is that the retention time of our MoS_2-based opto-synapse can be less than the corresponding time of three-terminal memories based on phase change[45] and the ferroelectric polarization[46] mechanism, which is attributed to the charge-hindering limitation of the interface barrier. The photo-induced carriers per synaptic event are determined by the various illumination times, which indicates the temporal information of the light pulse. As the light pulse time increases from 10 to 2,000 ms (P_{Light} = 0.147 mW cm^{-2}; Figure 4E), the peak values of ΔPSC exhibit a significant increasing trend from 44.3
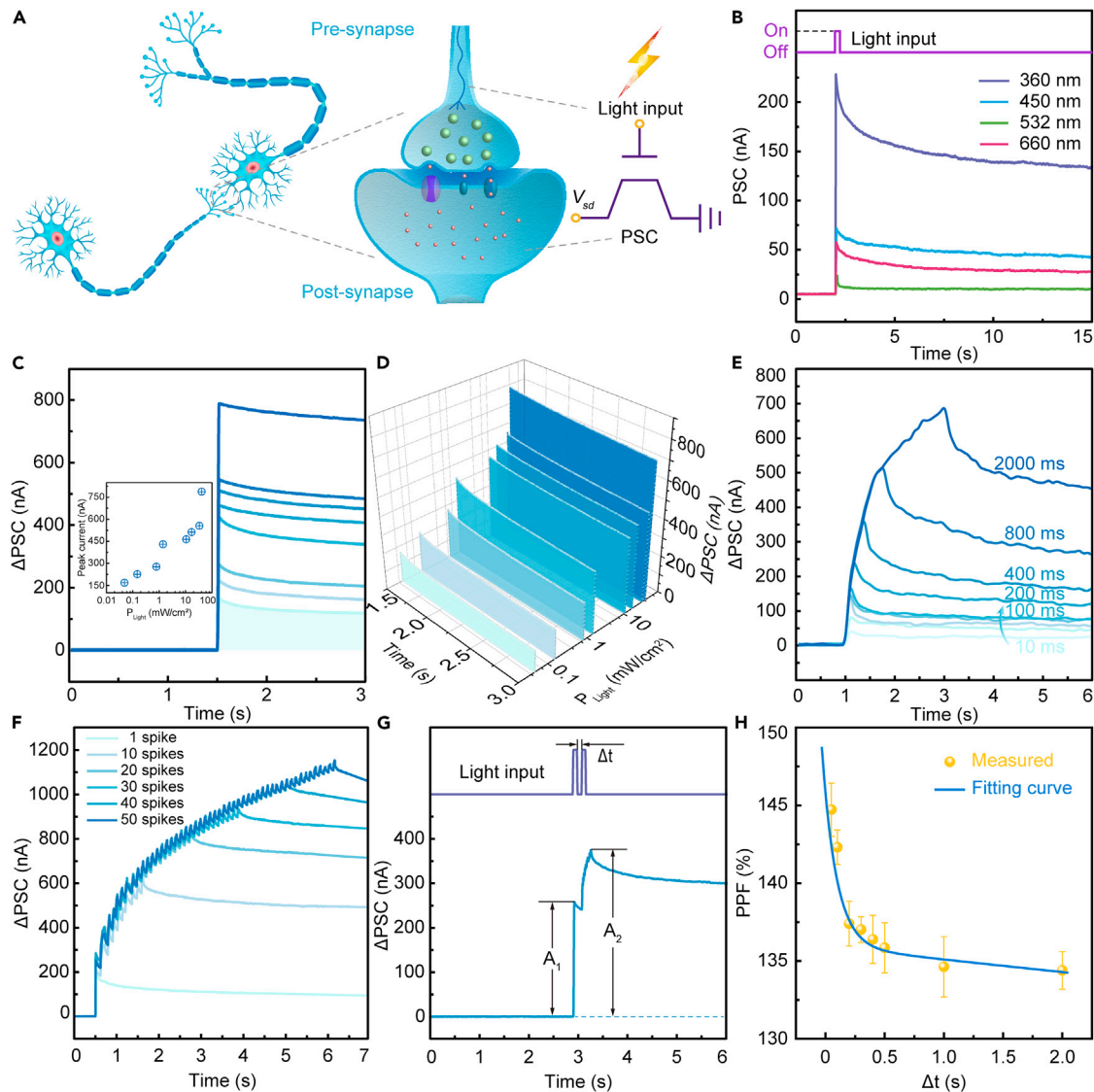
Figure 4. Emulation of the opto-synaptic features by the MoS$_2$ neuromorphic sensors

(A) Schematic illustration of nerve cells; signal transmission in biological synapse simplified mechanism of the light-stimulated artificial synaptic device.

(B) PSCs triggered by light pulses (wavelength: 360–660 nm, intensity of 0.147 mW cm^{-2}).

(C) ΔPSCs under various light intensities (360 nm, 0.048 to 40.70 mW cm^{-2}) at a light pulse width of 50 ms. Inset: the peak current of ΔPSC versus P_{Light}.

(D) ΔPSCs under different P_{Light}s when the light is turned off.

(E) ΔPSCs at different light pulse widths (360 nm, intensity of 0.147 mW cm^{-2}).

(F) ΔPSCs under 10 to 50 consecutive light pulses (360 nm, 0.147 mW cm^{-2}, pulse width of 50 ms).

(G) The ΔPSC triggered by a pair of presynaptic light pulses (360 nm, 0.147 mW cm^{-2}, Δt = 50 ms). A_1 and A_2 are the amplitudes of the first and second PSCs, respectively.

(H) PPF ratio plotted as the function of Δt with a fixed light pulse intensity of 0.147 mW cm^{-2} and a light pulse width of 50 ms.

Error bars in (H) represent standard errors from three independent tests of a synaptic transistor.

to 698 nA. Hence, synaptic excitatory behaviors can be optically modulated at a fixed bias voltage by both light intensity and illumination time. Figure 4F shows multiple conduction states of the synaptic device accumulated by stimuli of a series of 1–50 excitatory spikes (P_{Light}, 0.237 μW; pulse width, 50 ms; Δt = 50 ms), and the amplitude value of ΔPSC gradually increases from ~254.4 nA to ~1.158 μA. The learning process was rapid, while the current decay was comparatively delayed, indicating the long-term memory effect of the MoS$_2$-based

CellPress

opto-synapse. The gain value of ΔPSC (defined as A_n/A_1, where A is the amplitude of the ΔPSC peak value) reaches 455% after the stimulation of 40 consecutive light pulses (Figure S11).

Paired-pulse facilitation (PPF), as a typical short-term plasticity (STP) characteristic, occurs during neurotransmission, where the PSC is triggered by two sequential pulses, which also can be applied to evaluate the LTP behaviors for the opto-synapse. Figure 4G shows that the peak of the second PSC spike (A_2) is significantly larger than that of the first one (A_1). The PPF index of the opto-synapse can be expressed as

$$PPF = 100\% \times \frac{A_2}{A_1}, \qquad \text{(Equation 4)}$$

where A_1 and A_2 are the magnitudes of the first and second PSC peaks, respectively. The double-exponential function can be applied to effectively fit the PPF decay behavior of the devices:

$$PPF = 1 + C_1 \exp\left(-\frac{t}{\tau_1}\right) + C_2 \exp\left(-\frac{t}{\tau_2}\right), \qquad \text{(Equation 5)}$$

where t represents the interval time (Δt) between two sequential pulses and τ_1 and τ_2 are the characteristic relaxation times of two phases. Based on the fitting results, τ_1 and τ_2 were 115.6 ms and 41.86 s, respectively. This is quantitatively consistent with the timescales of biological synapses. In addition, benefitting from the enhancement of the flexophototronic effect, the opto-synapse also exhibits a prospective advantage with an incredible decrease in energy consumption to the femtojoule level (77.28 fJ/spike) with a high modulation efficiency ($\sim$28.6%) (Figure S12; Table S3; Note S6), which is far lower than conventional ion-gel-gated/floating-gated MoS$_2$-based memories (Table S4) and can compare with a human synapse (1–100 fJ).[21] Moreover, previous studies showed that the photoresponse speed of MoS$_2$-based photosensors can be in the picosecond scale.[47] Considering the FPS limit of human vision, the above-demonstrated artificial visual systems pave a path to potential applications such as real-time monitoring systems and dynamic detection with low consumption.

Image preprocessing and recognition

A distinguishing feature of the human retina is image preprocessing, which is crucial for enhancing the sensory data quality and improving the processing speed and accuracy of following tasks, such as image recognition and classification. The majority of visual information processed by present neuromorphic visual-perception systems is visible to human eyes. This is because visible light information is one of the primary categories for external information that direct human production and life. However, broadband spectra, including UV light, can also play important roles in biological behaviors and communication for humans and other animals. For example, butterflies may have a sexually dimorphic visual system,[48] where males perform better in UV-rich environments for finding healthy mates,[49] while females outperform males in distinguishing the inner UV-yellow corollas from outer orange petals to maximize nectar supply for the upcoming reproduction.[48] In addition, the retina can automatically filter out redundant information when selecting characteristic information from the picture or environment; for example, one sighted individual is easily able to pass an identification of the red-green vision defect by disregarding the extra noise and sharpening the specific symbol. This process involves noise reduction and contrast enhancement, and these two techniques are necessary to highlight the major feature information of an image for image preprocessing.

Designing an appropriate convolution kernel[50–52] as a matrix of weight values applied to conduct a weighted average operation over pixels within unit area, this information extraction can contribute to simulate the behaviors of butterflies utilizing UV information during mating and foraging, and we construct BIP arrays to present basal functions of image sensing, image noise reduction, and image contrast enhancement. Each MoS_2 visual sensor of the 3 × 3 array (Figure S13) can distinguish the UV signal from visible light according to the high photocurrent response to UV, thus realizing simple RGB noise reduction. The preprocessing broadband image datasets, shown in Figures 5A and S14, include four different letter types, namely, "U," "C," "A," and "S," and the results after the noise reduction processing correspond well to the target letters. However, there may be a weaker output induced by inadequate incident illumination, making it necessary to conduct contrast enhancement to further extract feature information. For the visual sensor, contrast enhancement can be realized by improving light dosage, namely increasing illumination time and enhancing light intensities. Figure S15 shows a simplified schematic of the illumination pattern and the light-dosage-tunable programming methods for this array. During this training process, we can regard light intensities as weights because the light-intensity dependence of photoresponsivity in each device exhibits a linear relationship over a broad range of illumination (Figure 3E). The photocurrent outputs are continuously optimized with the training proceeding (Figures S14 and S17), which is beneficial to realize contrast enhancement for information extraction.

The artificial visual system includes image preprocessing and recognition as shown in Figure 5B, and the standard Fashion-MNIST (FMNIST) dataset (with a size of 28 × 28 pixels each; Figure S18) was used to demonstrate the effects of preprocessing operations for UV feature information extraction in image recognition. This dataset provided more benefit to simulate retina-inspired neural networks than the conventional MNIST dataset, which was overused and easily trained. In the computer simulation, an extra value that was different from the RGB values was created to bring the invisible UV information into typical RGB images, and a convolution kernel (1 × 1 × 4) can conduct a weighted average operation over one pixel with four-color values (UV and RGB). Then, the preprocessed image was imported to a three-layer ANN to achieve the image training and recognition functions, which consisted of 784 input neurons, 128 hidden neurons, and 10 output neurons (as the right section of Figure 5B shows). Note S9 describes the detailed mechanisms of the convolution kernel and the ANN, in which nonlinearity values for depression can be obtained by gate-pulse inhibition to realize weight updates (Figure S16; Table S5; Note S8). For image recognition, 60,000 images from the FMNST training datasets were trained by means of the back-propagation algorithm for the ANN simulation, and then three different types of test datasets were inputted to the ANN to quantitatively evaluate the effect of the preprocessing operations. The test datasets contain the original FMNIST test dataset, the dataset after adding RGB Gaussian noise, and the dataset after preprocessing (Figures 5C and S19). Finally, Figure 5D shows the comparison of recognition accuracy among the datasets before training, and the results illustrate that the recognition accuracy of images, including RGB noise, slowly increased after ten training epochs and only reached 35% after 50 training epochs, which means that the feature information was hardly recognized by the visual system, whereas the image after preprocessing shows obvious improvements for recognition accuracy of 90% after 50 training epochs, which approaches the training results for the original datasets. The results demonstrate the availability of in-sensor BIP in the preprocess of extracting UV information functions.
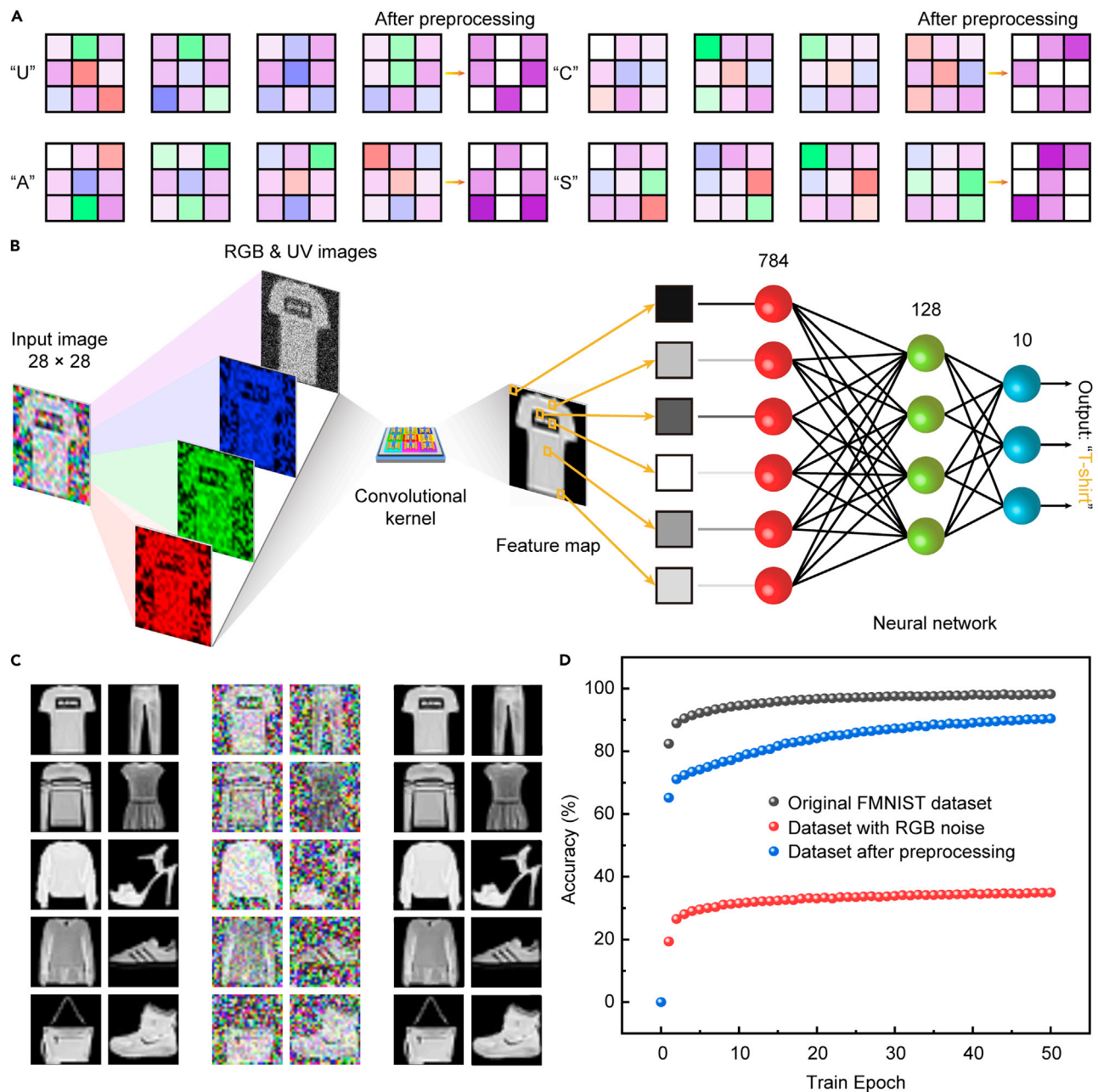
Matter
Article

CellPress

Figure 5. Image recognition using in-sensor BIP array

(A) Selective recognition of different types of letters ("U," "C," "A," and "S"), where purple, blue, green, and red represent UV (360 nm), blue (450 nm), green (532 nm), and red (660 nm) light, respectively.

(B) Realization of neuromorphic preprocessing function to achieve image noise reduction and contrast enhancement using the in-sensor BIP array. The system includes a convolution kernel array part for visual information preprocessing and an ANN part for image recognition.

(C) Three types of preprepared images including the original Fashion-MNIST test images (left columns), the images after adding RGB Gaussian noise (middle columns), and the images after neuromorphic preprocessing by the BIP array (right columns).

(D) Recognition accuracy with and without neuromorphic preprocessing.

Conclusions

In summary, we have successfully demonstrated a brand new neuromorphic visual system based on MoS_2 flexophototronic photosensors that can emulate the functions of the photoreceptors in the retina and the visual cortex. The device can

perceive and store broadband optical information due to the 3DSS effect and interface barrier, then simulate light-tunable synaptic characteristics with low energy consumption (77.28 fJ/spike). The broadband-tunable synaptic plasticity of the array enables the artificial visual system to execute image preprocessing, namely noise reduction and contrast enhancement, which significantly improve the efficiencies and accuracy of subsequent image recognition tasks, and the neuro-morphic arrays can increase the image recognition rate from 35% to 90% for FMNIST datasets. This retina-inspired in-sensor broadband image processing system could be of use in high-efficiency and multifunctional neuromorphic visual systems and opens an avenue to practical applications of flexophototronics (Figure S20; Note S10).

EXPERIMENTAL PROCEDURES

Resource availability

Lead contact

Junyi Zhai serves as the lead contact (jyzhai@binn.cas.cn).

Materials availability

This study did not generate new or unique reagents.

Data and code availability

All experimental data are available from the lead contact upon reasonable request.

Device fabrication

hBN microbeams, few-layer MoS_2 nanoflakes, and graphene sheets were all me-chanically exfoliated onto polydimethylsiloxane (PDMS) and transferred (Metatest, E1-M) onto a 280 nm SiO_2/Si substrate; here, multilayer MoS_2 nanoflakes were chosen to avoid the piezophototronic effect and crack formation. Source and drain electrodes were patterned by electron-beam lithography (EBL), and then Cr/Au (10/50 nm) electrodes were deposited by electron-beam evaporation. More detailed processes are shown in Figure S1 and Note S2 (the selection of materials).

Array fabrication

The flexophototronic-enhanced sensor array was fabricated by using UV lithography and the inductively coupled plasma (ICP) etching method. In view of the size limita-tion of 2D materials obtained by the mechanical exfoliation method, the 2D mate-rials such as hBN flake, MoS_2 thin film, and graphene sheet were grown by chemical vapor deposition (CVD) method and transferred via wetting transfer method. Optical images after each lithography/etching are shown in Figure S13.

AFM characterization

The AFM and Kelvin probe force microscopy (KPFM) measurements were conducted by MFP-3D AFM from Asylum Research, and the related data were obtained by an AFM tip (ASYELEC.01-R2, Asylum Research, Santa Barbara, CA, USA) under the tapping mode.

Raman characterization

Raman imaging was performed on an WITec alpha300R confocal Raman microscope (WITec). The system is equipped with a diode-pumped solid-state 532 nm laser, focusing on a sample with a ×100 objective (numerical aperture [NA] = 0.9). Fast Raman imaging was done with a 200 nm step size. The power of the excitation laser line was kept below 1.46 mW to avoid shifting of the Raman peaks and damaging of the MoS_2 sample.

Matter
Article

CellPress

FDTD solution simulation

The distribution and absorption spectra of electric fields were simulated by means of the Lumerical FDTD solution. The x and y axes adopted periodic boundary conditions while a perfectly matched layer (PML) was set for the z axis, and a 0.8 nm mesh was set to the smallest size for the structure. The electric-field distribution and absorption spectra of MoS_2 nanoflakes on SiO_2 and hBN substrate are simulated, where the absorption spectra of 2D MoS_2 were obtained by relative reflection spectra.

Optoelectronic measurements

The light illumination was applied using commercial multiwavelength laser (FC-360-980 nm), and a hand-held optical power/energy meter (PM100D) was used to measure the laser power. Electrical measurements were performed in the probe station by means of Keithley 4200. Pulsed voltage was output by Keithley 2400 to generate laser spikes and served as a gate-voltage pulse. All the above measurements were performed in ambient environment at room temperature.

SUPPLEMENTAL INFORMATION

Supplemental information can be found online at https://doi.org/10.1016/j.matt.2022.11.022.

AUTHOR CONTRIBUTIONS

Conceptualization, P.G., M.J., Z.L.W., and J.Z.; methodology, P.G., M.J., D.G., and J.Z.; investigation, P.G., M.J., and D.G.; writing – original draft, P.G., M.J., and D.G.; writing – review & editing, Z.L.W. and J.Z.; funding acquisition, Z.L.W. and J.Z.; resources, Z.L.W. and J.Z.; supervision, Z.L.W. and J.Z.

DECLARATION OF INTERESTS

The authors declare no competing interests.

REFERENCES

1. Park, H.L., Lee, Y., Kim, N., Seo, D.G., Go, G.T., and Lee, T.W. (2020). Flexible neuromorphic electronics for computing, soft robotics, and neuroprosthetics. Adv. Mater. *32*, 1903558. https://doi.org/10.1002/adma.201903558.

2. Kim, Y., Chortos, A., Xu, W., Liu, Y., Oh, J.Y., Son, D., Kang, J., Foudeh, A.M., Zhu, C., Lee, Y., et al. (2018). A bioinspired flexible organic artificial afferent nerve. Science *360*, 998–1003. https://doi.org/10.1126/science.aao0098.

3. Jung, Y.H., Park, B., Kim, J.U., and Kim, T.I. (2019). Bioinspired electronics for artificial sensory systems. Adv. Mater. *31*, 1803637. https://doi.org/10.1002/adma.201803637.

4. Kumar, M., Som, T., and Kim, J. (2019). A transparent photonic artificial visual cortex. Adv. Mater. *31*, 1903095. https://doi.org/10.1002/adma.201903095.

5. Chai, Y. (2020). In-sensor computing for machine vision. Nature *579*, 32–33. https://doi.org/10.1038/d41586-020-00592-6.

6. Choi, C., Choi, M.K., Liu, S., Kim, M.S., Park, O.K., Im, C., Kim, J., Qin, X., Lee, G.J., Cho, K.W., et al. (2017). Human eye-inspired soft optoelectronic device using high-density MoS_2-graphene curved image sensor array. Nat. Commun. *8*, 1664. https://doi.org/10.1038/s41467-017-01824-6.

7. Zhou, F., Zhou, Z., Chen, J., Choy, T.H., Wang, J., Zhang, N., Lin, Z., Yu, S., Kang, J., Wong, H.-S.P., et al. (2019). Optoelectronic resistive random access memory for neuromorphic vision sensors. Nat. Nanotechnol. *14*, 776–782. https://doi.org/10.1038/s41565-019-0501-3.

8. Zhou, F., and Chai, Y. (2020). Near-sensor and in-sensor computing. Nat. Electron. *3*, 664–671. https://doi.org/10.1038/s41928-020-00501-9.

9. Zhang, Z., Wang, S., Liu, C., Xie, R., Hu, W., and Zhou, P. (2022). All-in-one two-dimensional retinomorphic hardware device for motion detection and recognition. Nat. Nanotechnol.

17, 27–32. https://doi.org/10.1038/s41565-021-01003-1.

10. Ram, M.S., Persson, K.M., Irish, A., Jönsson, A., Timm, R., and Wernersson, L.E. (2021). High-density logic-in-memory devices using vertical indium arsenide nanowires on silicon. Nat. Electron. *4*, 914–920. https://doi.org/10.1038/s41928-021-00688-5.

11. Lee, S., Peng, R., Wu, C., and Li, M. (2022). Programmable black phosphorus image sensor for broadband optoelectronic edge computing. Nat. Commun. *13*, 1485. https://doi.org/10.1038/s41467-022-29171-1.

12. Ielmini, D., and Wong, H.S.P. (2018). In-memory computing with resistive switching devices. Nat. Electron. *1*, 333–343. https://doi.org/10.1038/s41928-018-0092-2.

13. Gilbert, L.E., and Singer, M.C. (1975). Butterfly ecology. Annu. Rev. Ecol. Syst. *6*, 365–395. https://www.jstor.org/stable/2096836.

14. Avilés, J.M., Parejo, D., and Rodríguez, J. (2011). Parental favouritism strategies in the asynchronously hatching european roller (coracias garrulus). Behav. Ecol. Sociobiol. *65*, 1549–1557. https://doi.org/10.1007/s00265-011-1164-8.

15. Douglas, R.H., and Jeffery, G. (2014). The spectral transmission of ocular media suggests ultraviolet sensitivity is widespread among mammals. Proc. Biol. Sci. *281*, 20132995. https://doi.org/10.1098/rspb.2013.2995.

16. Jia, M., Guo, P., Wang, W., Yu, A., Zhang, Y., Wang, Z.L., and Zhai, J. (2022). Tactile tribotronic reconfigurable p-n junctions for artificial synapses. Sci. Bull. *67*, 803–812. https://doi.org/10.1016/j.scib.2021.12.014.

17. Park, H.L., Kim, H., Lim, D., Zhou, H., Kim, Y.H., Lee, Y., Park, S., and Lee, T.W. (2020). Retina-inspired carbon nitride-based photonic synapses for selective detection of uv light. Adv. Mater. *32*, 1906899. https://doi.org/10.1002/adma.201906899.

18. Zhao, T., Zhao, C., Xu, W., Liu, Y., Gao, H., Mitrovic, I.Z., Lim, E.G., Yang, L., and Zhao, C.Z. (2021). Bio-inspired photoelectric artificial synapse based on two-dimensional ti₃c₂tₓ mxenes floating gate. Adv. Funct. Mater. *31*, 2106000. https://doi.org/10.1002/adfm.202106000.

19. Yao, B., Li, J., Chen, X., Yu, M., Zhang, Z., Li, Y., Lu, T., and Zhang, J. (2021). Non-volatile electrolyte-gated transistors based on graphdiyne/MoS₂ with robust stability for low-power neuromorphic computing and logic-in-memory. Adv. Funct. Mater. *31*, 2100069. https://doi.org/10.1002/adfm.202100069.

20. Wang, D., Zhao, S., Yin, R., Li, L., Lou, Z., and Shen, G. (2021). Recent advanced applications of ion-gel in ionic-gated transistor. npj Flex. Electron. *5*, 13. https://doi.org/10.1038/s41528-021-00110-2.

21. Purves, D., Augustine, G.J., Fitzpatrick, D., Hall, W.C., LaMantia, A.-S., McNamara, J.O., and Williams, S.M. (2004). Neuroscience (Sinauer Associates). https://doi.org/10.1212/01.WNL.0000154473.43364.47.

22. Yu, J., Yang, X., Gao, G., Xiong, Y., Wang, Y., Han, J., Chen, Y., Zhang, H., Sun, Q., and Wang, Z.L. (2021). Bioinspired mechano-photonic artificial synapse based on graphene/MoS₂ heterostructure. Sci. Adv. *7*, eabd9117. https://doi.org/10.1126/sciadv.abd9117.

23. Wadhwa, R., Agrawal, A.V., and Kumar, M. (2022). A strategic review of recent progress, prospects and challenges of MoS₂-based photodetectors. J. Phys. D Appl. Phys. *55*, 063002. https://doi.org/10.1088/1361-6463/ac2d60.

24. Roy, K., Padmanabhan, M., Goswami, S., Sai, T.P., Ramalingam, G., Raghavan, S., and Ghosh, A. (2013). Graphene-MoS₂ hybrid structures for multifunctional photoresponsive memory devices. Nat. Nanotechnol. *8*, 826–830. https://doi.org/10.1038/nnano.2013.206.

25. Guo, P., Jia, M., Guo, D., Wang, W., Zhang, Y., Ren, L., Yu, A., Wang, Z.L., and Zhai, J. (2022). Mechanical modulation of 2d electronic devices at atto-joule energy via flexotronic effect. Adv. Funct. Mater. *32*, 2202779. https://doi.org/10.1002/adfm.202202779.

26. Wang, Z.L. (2010). Piezotronic and piezophototronic effects. J. Phys. Chem. Lett. *1*, 1388–1393. https://doi.org/10.1021/jz100330j.

27. Wu, W., Wang, L., Yu, R., Liu, Y., Wei, S.H., Hone, J., and Wang, Z.L. (2016). Piezophototronic effect in single-atomic-layer MoS₂ for strain-gated flexible optoelectronics. Adv. Mater. *28*, 8463–8468. https://doi.org/10.1002/adma.201602854.

28. Choi, W., Cho, M.Y., Konar, A., Lee, J.H., Cha, G.B., Hong, S.C., Kim, S., Kim, J., Jena, D., Joo, J., and Kim, S. (2012). High-detectivity multilayer MoS₂ phototransistors with spectral response from ultraviolet to infrared. Adv. Mater. *24*, 5832–5836. https://doi.org/10.1002/adma.201201909.

29. Narvaez, J., Vasquez-Sancho, F., and Catalan, G. (2016). Enhanced flexoelectric-like response in oxide semiconductors. Nature *538*, 219–221. https://doi.org/10.1038/nature19761.

30. Yang, M.M., Kim, D.J., and Alexe, M. (2018). Flexo-photovoltaic effect. Science *360*, 904–907. https://doi.org/10.1126/science.aan3256.

31. Wu, W., Wang, L., Li, Y., Zhang, F., Lin, L., Niu, S., Chenet, D., Zhang, X., Hao, Y., Heinz, T.F., et al. (2014). Piezoelectricity of single-atomic-layer MoS₂ for energy conversion and piezotronics. Nature *514*, 470–474. https://doi.org/10.1038/nature13792.

32. Wang, Z.L. (2010). Piezopotential gated nanowire devices: piezotronics and piezo-phototronics. Nano Today *5*, 540–552. https://doi.org/10.1016/j.nantod.2010.10.008.

33. Kang, D., Pikhitsa, P.V., Choi, Y.W., Lee, C., Shin, S.S., Piao, L., Park, B., Suh, K.-Y., Kim, T.-i., and Choi, M. (2014). Ultrasensitive mechanical crack-based sensor inspired by the spider sensory system. Nature *516*, 222–226. https://doi.org/10.1038/nature14002.

34. Yamada, T., Hayamizu, Y., Yamamoto, Y., Yomogida, Y., Izadi-Najafabadi, A., Futaba, D.N., and Hata, K. (2011). A stretchable carbon nanotube strain sensor for human-motion detection. Nat. Nanotechnol. *6*, 296–301. https://doi.org/10.1038/nnano.2011.36.

35. Chee, S.S., Seo, D., Kim, H., Jang, H., Lee, S., Moon, S.P., Lee, K.H., Kim, S.W., Choi, H., and Ham, M.H. (2019). Lowering the Schottky barrier height by graphene/ag electrodes for high-mobility MoS₂ field-effect transistors. Adv. Mater. *31*, 1804422. https://doi.org/10.1002/adma.201804422.

36. Ju, L., Velasco, J., Huang, E., Kahn, S., Nosiglia, C., Tsai, H.Z., Yang, W., Taniguchi, T., Watanabe, K., Zhang, Y., et al. (2014). Photoinduced doping in heterostructures of graphene and boron nitride. Nat. Nanotechnol. *9*, 348–352. https://doi.org/10.1038/nnano.2014.60.

37. Ng, H.K., Xiang, D., Suwardi, A., Hu, G., Yang, K., Zhao, Y., Liu, T., Cao, Z., Liu, H., Li, S., et al. (2022). Improving carrier mobility in two-dimensional semiconductors with rippled materials. Nat. Electron. *5*, 489–496. https://doi.org/10.1038/s41928-022-00777-z.

38. Conley, H.J., Wang, B., Ziegler, J.I., Haglund, R.F., Pantelides, S.T., and Bolotin, K.I. (2013). Bandgap engineering of strained monolayer and bilayer MoS₂. Nano Lett. *13*, 3626–3630. https://doi.org/10.1021/nl4014748.

39. Liu, B., Liao, Q., Zhang, X., Du, J., Ou, Y., Xiao, J., Kang, Z., Zhang, Z., and Zhang, Y. (2019). Strain-engineered van der Waals interfaces of mixed-dimensional heterostructure arrays. ACS Nano *13*, 9057–9066. https://doi.org/10.1021/acsnano.9b03239.

40. Liu, X., Hu, S., Luo, J., Li, X., Wu, J., Chi, D., Ang, K.W., Yu, W., and Cai, Y. (2021). Suspended MoS₂ photodetector using patterned sapphire substrate. Small *17*, 2100246. https://doi.org/10.1002/smll.202100246.

41. Chakraborty, B., Matte, H.S.S.R., Sood, A.K., and Rao, C.N.R. (2013). Layer-dependent resonant Raman scattering of a few layer MoS₂. J. Raman Spectrosc. *44*, 92–96. https://doi.org/10.1002/jrs.4147.

42. Rice, C., Young, R.J., Zan, R., Bangert, U., Wolverson, D., Georgiou, T., Jalil, R., and Novoselov, K.S. (2013). Raman-scattering measurements and first-principles calculations of strain-induced phonon shifts in monolayer MoS₂. Phys. Rev. B *87*, 081307. https://doi.org/10.1103/PhysRevB.87.081307.

43. Lopez-Sanchez, O., Lembke, D., Kayci, M., Radenovic, A., and Kis, A. (2013). Ultrasensitive photodetectors based on monolayer MoS₂. Nat. Nanotechnol. *8*, 497–501. https://doi.org/10.1038/nnano.2013.100.

44. Yang, C., Qian, J., Jiang, S., Wang, H., Wang, Q., Wan, Q., Chan, P.K.L., Shi, Y., and Li, Y. (2020). An optically modulated organic Schottky-barrier planar-diode-based artificial synapse. Adv. Opt. Mater. *8*, 2000153. https://doi.org/10.1002/adom.202000153.

45. Pickett, M.D., Medeiros-Ribeiro, G., and Williams, R.S. (2013). A scalable neuristor built with mott memristors. Nat. Mater. *12*, 114–117. https://doi.org/10.1038/nmat3510.

46. Pei, M., Qian, J., Jiang, S., Guo, J., Yang, C., Pan, D., Wang, Q., Wang, X., Shi, Y., and Li, Y. (2019). Pj-level energy-consuming, low-voltage ferroelectric organic field-effect transistor memories. J. Phys. Chem. Lett. *10*, 2335–2340. https://doi.org/10.1021/acs.jpclett.9b00864.

47. Wang, H., Zhang, C., Chan, W., Tiwari, S., and Rana, F. (2015). Ultrafast response of monolayer molybdenum disulfide photodetectors. Nat. Commun. *6*, 8831. https://doi.org/10.1038/ncomms9831.

48. Finkbeiner, S.D., and Briscoe, A.D. (2021). True uv color vision in a female butterfly with two uv opsins. J. Exp. Biol. *224*, jeb242802. https://doi.org/10.1242/jeb.242802.

49. Obara, Y., Koshitaka, H., and Arikawa, K. (2008). Better mate in the shade: enhancement of male mating behaviour in the cabbage butterfly, pieris rapae crucivora, in a uv-rich environment. J. Exp. Biol. *211*, 3698–3702. https://doi.org/10.1242/jeb.021980.

50. Oh, S., Shi, Y., del Valle, J., Salev, P., Lu, Y., Huang, Z., Kalcheim, Y., Schuller, I.K., and Kuzum, D. (2021). Energy-efficient mott activation neuron for full-hardware implementation of neural networks. Nat. Nanotechnol. *16*, 680–687.

https://doi.org/10.1038/s41565-021-00874-8.

51. Pi, L., Wang, P., Liang, S.J., Luo, P., Wang, H., Li, D., Li, Z., Chen, P., Zhou, X., Miao, F., et al. (2022). Broadband convolutional processing using band-alignment-tunable heterostructures. Nat. Electron. *5*, 248–254. https://doi.org/10.1038/s41928-022-00747-5.

52. Wang, C.Y., Liang, S.J., Wang, S., Wang, P., Li, Z., Wang, Z., Gao, A., Pan, C., Liu, C., Liu, J., et al. (2020). Gate-tunable van der Waals heterostructure for reconfigurable neural network vision sensor. Sci. Adv. *6*, eaba6173. https://doi.org/10.1126/sciadv.aba6173.